# Dynamical Instability in a Trimeric Chain of Interacting Bose-Einstein Condensates

# Dynamical instability in a trimeric chain of interacting Bose-Einstein condensates

P. Buonsante,[1] R. Franzosi,[2] and V. Penna[1,*]

[1]*Dipartimento di Fisica and U.d.R. I.N.F.M., Politecnico di Torino, Corso Duca degli Abruzzi 24, I-10129 Torino, ITALIA*

[2]*Dipartimento di Fisica, Università degli Studi di Pisa and I.N.F.N., Sezione di Pisa, Via Buonarroti 2, I-56127 Pisa, ITALIA*

(Dated: September 17, 2018)

We analyze thoroughly the mean-field dynamics of a linear chain of three coupled Bose-Einstein condensates, where both the tunneling and the central-well relative depth are adjustable parameters. Owing to its nonintegrability, entailing a complex dynamics with chaos occurrence, this system is a paradigm for longer arrays whose simplicity still allows a thorough analytical study.We identify the set of dynamics fixed points, along with the associated proper modes, and establish their stability character depending on the significant parameters. As an example of the remarkable operational value of our analysis, we point out some macroscopic effects that seem viable to experiments.

PACS numbers: 03.75.Fi, 05.45.-a, 03.65.Sq

Since the first realizations [1] of Bose-Einstein condensation in atomic gases, great efforts have been aimed at improving the control of geometrical arrangements of the condensate and, in particular, at realizing its fragmentation in many interacting components. The design of increasingly efficient trapping schemes [2, 3, 4] has shown this program to be a fairly realistic perspective. Indeed experiments involving Bose-Einstein condensates (BEC) distributed within optical traps were successfully conducted that provided quite large 1D [5] and 2D [6] periodic arrays interacting via tunneling. Based on magnetic trapping [7] the simplest case, consisting of two coupled condensates (dimer), was realized as well. In parallel, the rich scenario of phenomena observed in BECs arrays (nonlinear oscillations [8], self-trapping [9], supercurrents [10], and solitons [11, 12]) raised a number of questions on their time evolution. The possibility to detect and study, both experimentally and theoretically, new macroscopic dynamical phenomena/effects in BEC arrays (thus getting a deeper insight of stability properties and, operatively, an increased control of systems) has prompted an intense ongoing work.

In this perspective, the three-site array (trimer) deserves a special attention. According to the standard mean-field treatment, which is fairly satisfactory when the average well populations are large [13], the dimer dynamics is integrable [14]. The latter is described by two macroscopic complex variables $z_i = |z_i| \exp(i\vartheta_i)$, accounting for the condensates' state (phase $\vartheta_i$ and population $|z_i|^2$), and exhibits two constants of motion, namely the total boson number and the energy. The apparently harmless addition of a further coupled condensate is sufficient to make the system nonintegrable thus causing, in the presence of nonlinear BEC self-interactions, strong instabilities in extended regions of the phase space [15]. That is, while keeping simple enough to be viable to a thorough analytical study, the system displays a whole new class of behaviors which, though often overlooked, are typical of longer arrays. Moreover, the recent achievements in the experimental field – and especially the control promised by micro traps [4] – suggest the realization of the trimer to be at hand. For all these reasons we feel that the trimer deserves a systematic analysis, whose key results we discuss below.

We consider an asymmetric open trimer (AOT) made of three coupled BECs arranged into a row, where both the interwell tunneling $T$ and the central-well relative depth $w$ are adjustable parameters. Compared with the symmetric case [16] (trimer on a closed chain of equal-depth wells), the interplay of such parameters both entails a deeper control on the dynamics and favours the approach to experimental situations. After recognizing the location of fixed points in the phase space and the associated proper modes, we focus mostly on establishing via standard methods their *stability character* on varying $\tau = T/UN$ and $\nu = w/UN$, where $U$ embodies the interatomic scattering and $N$ is the total boson number. Also, we show how macroscopic (i.e. interesting experimentally) dynamical effects can be primed by selecting suitable critical values of $\tau$ and $\nu$.

The essential physics of the AOT is aptly described [13, 17] by the Bose-Hubbard Model, which represents a gas of identical bosons hopping across an ambient lattice. The relevant Hamiltonian, ensuing from the boson field theory through the *space-mode* approximation of field operators [18], reads $H = \Sigma_{k=1}^{3}(Un_k^2 - vn_k) - wn_2 - T[a_2^+(a_1 + a_3) + \text{h.c.}]/2$, where $v$ is the depth of wells $j = 1, 3$ ($w$, $T$, $U$ are defined above), $n_i = a_i^+ a_i$ counts the bosons at site $i$, and the destruction (creation) operators $a_i$ ($a_i^+$) obey commutators $[a_i, a_h^+] = \delta_{ih}$. If the well populations are not so small that a purely quantum treatment is in order, the system dynamics can be described by three variables $z_i$ within the mean-field picture. This is recovered via the coherent-state variational procedure of Ref. 17, where the semiclassical Hamiltonian $\mathcal{H} = \Sigma_{k=1}^{3}(U|z_k|^4 - v|z_k|^2) - w|z_2|^2 - T/2[z_2^*(z_1 + z_3) + \text{c.c.}]$ is derived from the system effective action $S(t)$ ensuing in turn from the macroscopic trial state $|\Psi\rangle = \exp(iS/\hbar)\,\Pi_i\,|z_i\rangle$, written in terms of the Glauber's coherent states, $a_j|z_j\rangle = z_j\,|z_j\rangle$. In this frame-

work the symbol $n_i$ is used to denote the expectation value $\langle\Psi|n_i|\Psi\rangle = |z_i|^2$. Equipped with the Poisson brackets $\{z_j^*, z_h\} = i/\hbar\,\delta_{jh}$, $\mathcal{H}$ yields the dynamical equations,

$$\begin{cases} i\hbar\dot{z}_j = (2U|z_j|^2 - v)\,z_j - \frac{T}{2}z_2 \\ i\hbar\dot{z}_2 = (2U|z_2|^2 - v - w)\,z_2 - \frac{T}{2}\,(z_1 + z_3) \end{cases}, \quad (1)$$

with $j = 1, 3$ in the first equation. Eqs. (1) incorporate the conservation of total boson number $N = \Sigma_{j=1}^{3}|z_j|^2$, since $\{N, \mathcal{H}\} = 0$, and provide, by conjugation, the equations for $\{z_k^*\}$. Further, they propagate in time the initial condition $z_1 = z_3$, thus revealing an integrable subregime characterized by the first integrals $\mathcal{H}$ and $N = 2|z_1|^2 + |z_2|^2$: We refer to such a regime as the *dimeric* regime (DR), as opposed to the *nondimeric* regime (NR) where $z_1 \neq z_3$.

The distinctive features characterizing a given Hamiltonian dynamics are deduced by exploring its phase-space structure. This is attained in the first place by working out the location and the local character of its fixed points. For Eqs. (1), the latter are issued from

$$\begin{cases} 0 = (2U|z_j|^2 - \mu)\,z_j - \frac{T}{2}z_2 & j = 1, 3 \\ 0 = (2U|z_2|^2 - \mu - w)\,z_2 - \frac{T}{2}\,(z_1 + z_3) \end{cases} \quad (2)$$

where $\mu = v + \chi$ and $\chi$ is a Lagrange multiplier selecting the conserved value of $N$. Every solution $(\eta_1, \eta_2, \eta_3)$ of Eqs. (2) naturally provides a periodic solution of Eqs. (1) of the form $z_j(t) = \eta_j\,\exp[i\,\chi\,t/\hbar]$. The global phase symmetry $z_j \mapsto z_j\,\exp[i\,\Phi]$ ($\Phi \in [0, 2\,\pi]$) allows one to replace $z_i$ with $x_i \in \mathbb{R}$ thus reducing system (2) to

$$\begin{cases} 0 = (2\,x_j^2 - m)x_j - \frac{\tau}{2}\,x_2 & j = 1, 3 \\ 0 = (2\,x_2^2 - m - \nu)\,x_2 - \frac{\tau}{2}\,(x_1 + x_3) \end{cases} \quad (3)$$

where $m = \mu/UN$, and $\mathbf{x}^t = (x_1, x_2, x_3)$ is such that $z_j = \sqrt{N}x_j\,\exp[i\,\Phi]$ and $\Sigma_i x_i^2 = \Sigma_i n_i/N = 1$. Notice that the structure of system (3) entails that the solution where either one or both of the peripheral sites are depleted is trivial: $x_{1,3} = 0 \Rightarrow \mathbf{x} = \mathbf{0}$. The situation where the central well is depleted, henceforth referred to as *central-depleted well* (CDW) yields $x_1 = -x_3 = \pm\sqrt{m/2} = \pm 1/\sqrt{2}$. Note that this represents the trimeric counterpart of dimer $\pi$-states [8]. In general, except for the simple CDW case, solving system (3) for $\tau \neq 0$ is found to be equivalent to finding the real roots of the quartic polynomial in $\alpha$ [20]

$$\mathcal{P}_{\tau\nu}(\alpha) = \alpha^4 + b_{\tau\nu}\alpha^3 + c_{\tau\nu}\alpha + d = 0, \quad (4)$$

Once a solution is found in terms of $\alpha$, the relevant configuration $\mathbf{x}$ is recovered as $x_2 = \alpha R(\alpha)/\sqrt{1+\alpha^2}$,

$$x_{1,3} = (X_1 \pm X_3)/\sqrt{2}\ \ (\mathrm{NR}), \quad x_{1,3} = X_{1,3}\ \ (\mathrm{DR}) \quad (5)$$

where $X_3 = (1 - X_1^2 - x_2^2)^{\frac{1}{2}}$, $X_1 = R(\alpha)/\sqrt{1+\alpha^2}$ and $R(\alpha) = (1 - \tau\,\alpha/\sqrt{8})^{\frac{1}{2}}$ in the NR, while $X_1 = R(\alpha)/\sqrt{2\,(1+\alpha^2)}$, $R(\alpha) = 1$ in the DR.

The study of Eq. (4) allows one to construct the upper-panel diagrams of Figs. 1 and 2, where the same shade of gray characterizes regions of the $\tau\nu$ plane featuring the same number of fixed points. Also, it represents an essential element in building the *stability diagrams* [displayed in the lower panel of Fig. 1 (Fig. 2) for the DR (NR)] which are the central result of this letter. Operationally, such diagrams, depicted in the $\theta\tau$ plane (where $\theta = \arctan(\alpha) \in [-\pi/2, \pi/2]$), allow to determine both the location and the stability character of the fixed points. For a given parameter pair $(\tilde{\tau}, \tilde{\nu})$, the latter are obtained by intersecting the straight line $\tau = \tilde{\tau}$ and the curve $\tau = \tau_{\tilde{\nu}}(\theta)$, where $\tau = \tau_\nu(\theta)$ is implicitly defined by equation $\mathcal{P}_{\tau\nu}(\alpha) = 0$. The fixed-point components $x_i$'s are obtained from the relevant $\theta$ via Eqs. (5). The lower panel of Fig. 1 (2) displays the graph of $\tau = \tau_\nu(\theta)$ for five (four) choices of $\nu$, which we discuss below. We remark that such diagrams embody the whole information on trimer dynamics. There, the fixed points are identified as maxima, minima and (stable/unstable) saddles based on the shade of gray of the region they lie in.

**Fixed-points local character**. This is identified analytically through a standard study of the signature of the quadratic form associated to a given Hamiltonian, along the lines of Ref. 16. Locally, to the second order in the displacements $\xi_j = \sqrt{N}\,(q_j + i\,p_j) = z_j - \zeta_j$ around the fixed point $\zeta_j = \sqrt{N}x_j$, one gets $\mathcal{H}(z_j) - \chi\,N = \mathcal{H}(\zeta_j) + U\,N^2\tau\,h(\mathbf{q}, \mathbf{p})/2$, with $\mathbf{q}^t = (q_1, q_2, q_3)$, $\mathbf{p}^t = (p_1, p_2, p_3)$ and $h(\mathbf{q}, \mathbf{p}) = \mathbf{q}^t Q\mathbf{q} + \mathbf{p}^t P\mathbf{p}$. Remarkably, the six-by-six matrix relevant to the quadratic form $h(\mathbf{q}, \mathbf{p})$ in the vicinity of a fixed point, *separates* into two three-by-three symmetric submatrices $P$, $Q$ depending on the $x_j$'s, $\tau$ and $\nu$. Also, when the displacements' constraint $\mathbf{x}^t\mathbf{q} = 0$ (issued from $\Sigma_j|z_j|^2 \equiv N$) is accounted for, the rank of $Q$ further reduces to two. Likewise only two eigenvalues of $P$ affect the fixed-point character, the third one being identically zero. Indeed it is easy to check that the relevant eigenvector is $\mathbf{p}_0 \propto \mathbf{x}$. The non-zero eigenvalues of $P$ have opposite signs in the CDW configuration (which is therefore a saddle), and the signs of $x_1/x_2$ and $x_3/x_2$ otherwise. Hence the character of a fixed point depends on the signs of the two pairs of significant eigenvalues of $P$ and $Q$.

**Linear stability analysis**. The linear stability [21] of the fixed point can be determined by studying the evolution of the displacements $\mathbf{q}$ and $\mathbf{p}$. This is governed by the differential equations $\dot{\mathbf{q}} = \{\mathbf{q}, \mathcal{H}\} = \sigma\,P\,\mathbf{p}$ and $\dot{\mathbf{p}} = \{\mathbf{p}, \mathcal{H}\} = -\sigma\,Q\,\mathbf{q}$ (with $\sigma = UN\tau/2\hbar$), through the Poisson brackets $\{q_j, p_k\} = \delta_{jk}/(2\,N\hbar)$ stemming from the original ones $\{z_j^*, z_k\} = i\delta_{j,k}/\hbar$. Such $\mathbf{qp}$ equations provide the dynamical six-by-six matrix $\mathbf{M_6}$ with diagonal (three-by-three) blocks vanishing, and off-diagonal blocks that coincide with matrices $P$ and $-Q$ [22].

Based on the standard criteria, a fixed point is (linearly) stable when none of the six complex eigenvalues $\{\lambda_j\}_{j=1}^{6}$ inherent in $\mathbf{M_6}$ features a positive real part. Otherwise the fixed point is *unstable* and a chaotic behavior may arise. The $\lambda_i$'s are conveniently obtained as the square roots of the eigenvalues $\{\Lambda_j\}_{j=1}^{3}$ of $-PQ$. Indeed, due to the block off-diagonal form of $\mathbf{M_6}$ and to the symmetry of $P$ and

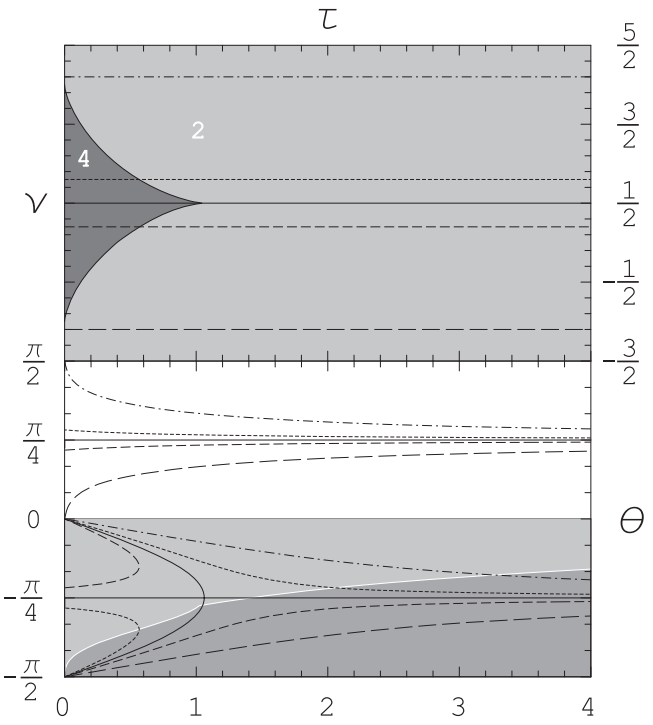


FIG. 1: Stability diagram for the DR. Upper panel: number of fixed points. Lower panel: character of the fixed points. The color keys of both panels, sharing the same $\tau$ axis, are the same as in the GR case (see caption of Fig. 2).

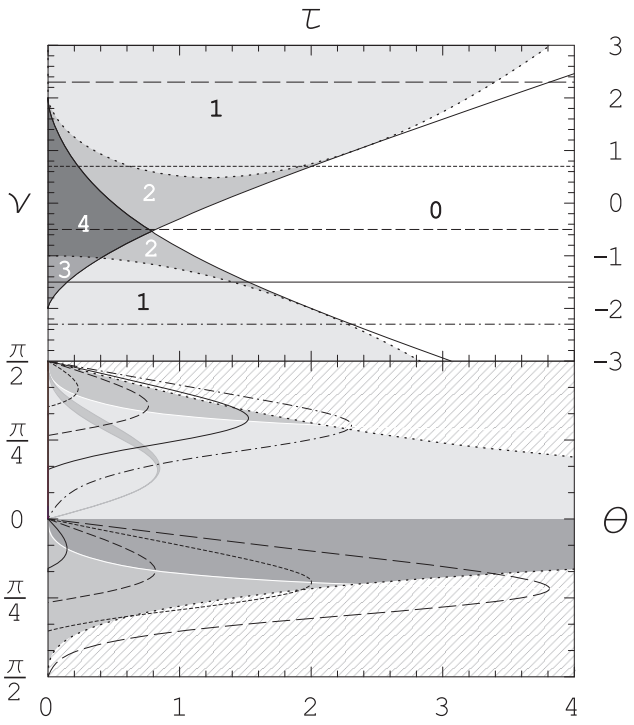


FIG. 2: Stability diagram for the NR. Upper panel: number of fixed points. The darker is a region, the larger is the relevant number of solutions, also displayed. The lines at a fixed value of $\nu$ correspond to the curves $\tau_\nu(\theta)$ appearing in the lower panel with the same dashing style. Lower panel: character of the fixed points. Dark gray: maxima; Medium gray: unstable saddles; Light Gray: stable saddles (only in the NR); White: minima (only in the DR); Diagonal lines: forbidden regions (only in the NR). Both panels share the same $\tau$ axis.

$Q$, $\det(\lambda-\mathbf{M_6})=\det(\lambda^2+PQ)$. As expected, this implies that maxima and minima are stable points. Indeed for such configurations the eigenvalues of $P$ and $Q$ have the same signs (non-positive for the maxima and non-negative for the minima), yielding therefore non-positive $\Lambda_j$'s and purely imaginary $\lambda_j$'s. Further, the fact that one of the eigenvalues of $P$ is zero implies that one of the $\Lambda_j$'s, and hence two of the $\lambda_j$'s, are zero as well. The four remaining $\lambda_j$'s are the roots of a biquadratic polynomial of the form $\lambda^4-s\lambda^2+p$. A fixed point is therefore stable if the conditions $s^2-4p<0$, $p>0$ and $s<0$ are simultaneously met.

**Discussion**. The character/stability of fixed points are fully described by the lower panel of Fig. 1 (Fig. 2) – referred to the DR (NR)– through the graphs of function $\tau_\nu(\theta)$ for five (four) significant choices of $\nu$, distinguished by different dashing patterns. In the figure upper panels a straight horizontal line featuring the same dashing style as the corresponding $\tau_\nu(\theta)$ curve allows one to read the relevant value of $\nu$. As noted above, each pair $(\bar\nu,\bar\tau)$ selects the set $\{\theta_r : \bar\tau=\tau_{\bar\nu}(\theta_r),\, r\le 4\}$ giving the fixed-point components. Depending on the shade of gray filling the region it lies in, a fixed point is either a minimum (white), a stable/unstable saddle point (light/medium gray) or a maximum (dark gray). In the DR (Fig. 1) each curve $\tau_\nu(\theta)$ has two branches featuring asymptotes at $\theta=\pm\pi/4$. For $-1\le\nu\le 2$, a third bell-shaped branch [see $\tau_\nu(\theta)$ for $\nu=0.2, 0.4$] crops up. Hence the DR always has two fixed points, of which one is always a minimum, whereas the other is a maximum (unstable saddle) for large (small) $\tau$'s. For $\nu=1/2$ the unbounded branches actually collapse on their asymptotes, thus providing $\tau$-independent solutions [23]. In the NR, Fig. 2, $\tau_\nu(\theta)$ features one or two bell-shaped branches, depending on whether $|\nu|\ge 2$ or $|\nu|<2$, respectively. Notice that in some cases entire portions of such branches, namely the ones lying within the patterned regions, must be discarded since, despite they are real, the relevant roots of polynomial (4) yield complex solutions of system (3). The dotted curves appearing in the upper panel of Fig. 2 are actually the counterparts of the dotted curves delimiting such forbidden regions, and significantly modify the simpler picture ensuing from the mere study of the real roots of polynomial (4) (solid black lines). For $\tau<2[2/3^{1/2}-1]^{1/2}$ and $\nu$ ranging around $\nu=2(3^{1/2}-2)$ a four-solution lobe is found. As observed above, maxima and minima are predicted to be stable fixed points. Noticeably, the stability analysis evidences that in the NR a significant fraction of the saddle points is dynam-

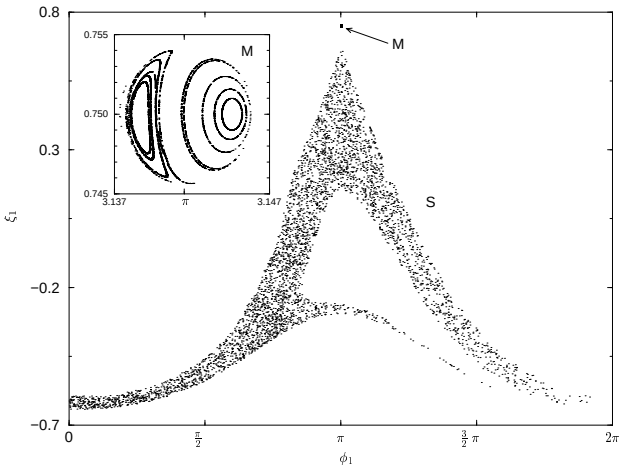


FIG. 3: Sets S and M of Poincaré sections of trajectories based close to $C_0$ for two choices of significant parameters $\tau, \nu$ (see the text for further detail). Sections are cut at $\xi_2 = -3/4$ within the reduced phase space $(\xi_1, \xi_2, \phi_1, \phi_2)$, [with $\xi_1 = (n_3 - n_1 + n_2)/N$, $\xi_2 = (n_3 - n_1 - n_2)/N$] ensuing from $\dot{N} = 0$ (see also Ref. 16).

ically stable (light gray), while in the DR the saddle points are always unstable (medium gray). Also, while Fig. 1 shows how the minimum always belongs to the DR, the absolute maximum is found either in the DR or in the NR depending on the values of $\nu$, $\tau$. As to the CDW saddle, it is unstable in the region $\{\nu < -1, \tau \leq \sqrt{-1-\nu}\} \cup \{|\nu| < 1, \tau \geq [(1+\nu)^3/(2-2\,\nu)]^{\frac{1}{2}}\}$ and stable elsewhere.

As already mentioned, the versatility of micro traps [4] promises a full control on the features of the trapping potentials, and hence on the parameters $\tau$ and $\nu$. It is worth noting that present experimental setups [5, 6] already allow to tune the ratio $T/U$ so that, according to the estimates in Ref. 18, $\tau$ spans the range displayed in Figs. 1 and 2 if a macroscopic $N = 10^3 \div 10^5$ is considered [24].

We conclude by emphasizing two interesting features of AOT, among the many suggested by our analysis, which seem to be more readily apt to experimental tests. As to the just mentioned CDW saddle we recall that its form ($n_2 = 0$, counter-phased side wells with $n_1 = n_3$) does not depend on parameters $\tau$ and $\nu$. Hence a system prepared in such a configuration with a weak ($\tau \ll 1$) inter-well tunneling, would remain in such apparently unnatural state also when tunneling is enhanced ($\tau \gg 0$), provided the central well is sufficiently deep ($\nu > 1$) to ensure the dynamical stability of the fixed point. Notice that preparing two separate counterphased condensates is by no means an easy task. In this respect the above described phenomenology suggests an operational method to check if the system is satisfactorily close to the desired configuration. Further, we remark that, owing to the relatively simple algebraic structure of the dimeric equations, there exists a simple, actually linear, functional relation among $\tau$ and $\nu$ ensuring that a fixed point is characterized by the same coordinates $x_i$'s independent of the parameters [25]. This allows one to evaluate with little effort different sets of parameters $(\tau, \nu)$ for which the same fixed point belongs to regions having a different stability character. Then, a relatively simple tuning of $\tau$ and $\nu$ leads to change the fixed-point character from stable to unstable, thus inducing chaos onset. Such an effect is manifest in Fig. 3, where two sets (labeled by $M$ and $S$) of Poincaré sections, both issued from initial conditions quite close to the configuration $C_0$ ($n_1 = n_3 = N/8$, $n_2 = 3/4N$, $\phi_1 = \vartheta_2 - \vartheta_1 = \pi$, $\phi_2 = \vartheta_3 - \vartheta_2 = -\pi$) are plotted for $(\tau_{\rm M}, \nu_{\rm M}) = (7/[4\sqrt{6}], 2/3)$ and $(\tau_{\rm S}, \nu_{\rm S}) = (13/[8\sqrt{6}], 17/24)$, so that the corresponding points $(\tau_{\rm M,S}, \theta = -\pi/3)$ lie just in the maxima and the saddle regions, respectively. Notice indeed that the former parameter choice yields the regular section expected for a stable point. Conversely, when the fixed point is a saddle, trajectories based very close to it invade a large phase-space region, as testified by Fig. 3 where the relevant Poincaré sections are undistinguishably merged into a fuzzy cloud of points. The analytical study exposed in the present letter is widely confirmed by numerical simulations where the chaoticity of the unstable fixed points is manifest. A thorough discussion of the AOT phenomenology and of further macroscopic effects disclosed by the stability diagrams will be presented in a later paper [24].

* corresponding author. Mailto: vittorio.penna@polito.it


[1] M. H. Anderson et al., Science **269**, 198 (1995).
[2] B. Anderson and M. Kasevich, Science **282**, 1686 (1998).
[3] N. R. Thomas et al., Phys. Rev. A **65**, 063406 (2002).
[4] H. Ott et al., Phys. Rev. Lett. **87**, 230401 (2001); W. Hänsel et al., Nature **413**, 498 (2001); J. Reichel, Appl. Phys. B **75**, 469 (2002).
[5] P. Pedri et al., Phys. Rev. Lett. **87**, 220401 (2001); O. Morsch et al., *ibid*. **87**, 140402 (2001).
[6] M. Greiner et al., Phys. Rev. Lett. **87**, 160405 (2001).
[7] M. R. Andrews et al., Science **275**, 637 (1997).
[8] A. Smerzi et al., Phys. Rev. Lett. **79**, 4950 (1997).
[9] G. J. Milburn et al., Phys. Rev. A **55**, 4318 (1997).
[10] S. Burger et al., Science **287**, 97 (2000).
[11] B. P. Anderson et al., Phys. Rev. Lett. **86**, 2926 (2001).
[12] J. Denschlag et al., Science **287**, 97 (2000).
[13] R. Franzosi et al., Int. J. Mod. Phys. B **14**, 943 (2000).
[14] S. Aubry et al., Phys. Rev. Lett. **76**, 1607 (1996).
[15] Here we treat the integrability of the mean field approximation of the BEC dynamics. Recent work on the issue of quantum integrability of coupled BEC can be found in: H.-Q. Zhou et al, cond-mat/0203009; cond-mat/0207540.
[16] R. Franzosi and V. Penna, cond-mat/0203509.
[17] L. Amico and V. Penna, Phys. Rev. Lett. **80**, 2189 (1998).
[18] D. Jaksch et al., Phys. Rev. Lett. **81**, 3108 (1998).
[19] W.-M. Zhang et al., Rev. Mod. Phys **62**, 867 (1990).
[20] NR: $b_{\tau\nu} = 2\sqrt{2}(\nu-2)/(3\tau)$, $c_{\tau\nu} = 4\sqrt{2}\,(\nu+2)/(3\tau)$, $d = 4/3$; DR: $b_{\tau\nu} = \sqrt{2}(2-\nu)/\tau$, $c_{\tau\nu} = -\sqrt{2}\,(\nu+1)/\tau$, $d = -1$.

[21] E. Ott, *Chaos in Dynamical Systems*, Cambridge University Press, 1993.

[22] The block structure of both the Hessian and $\mathbf{M_6}$ is ultimately due to the global phase symmetry. Further, the always true condition $P\mathbf{x}=0$ ensures the time-propagation of the displacements' constraint: $d(\mathbf{x}^t\mathbf{q})/dt \propto \mathbf{x}^t P\mathbf{p}=0$.

[23] This is related to the peculiar symmetry of system (3), characterizing the DR ($x_1 = x_3$): $\{(\bar{x}_1, x_2); \tilde{\nu}\} \leftrightarrow \{(\bar{x}_1, x_2); -\tilde{\nu}\}$, where $\tilde{\nu} = \nu - 1/2$ and $\bar{x}_1 = \sqrt{2}x$.

[24] P. Buonsante et al., (2002), in preparation.

[25] In the generic regime such functional relation is complicated essentially by the dependance of $R$ on $\theta$ and $\tau$.